EINDHOVEN UNIVERSITY OF TECHNOLOGY

Fiber-induced crystallization in elongational flows

Citation for published version (APA):
van Heugten, P. M. H., Looijmans, S. F. S. P., van Berlo, F. P. A., Rosenthal, M., Anderson, P. D., & van Breemen, L. C. A. (2024). Fiber-induced crystallization in elongational flows. *Macromolecules*, *57*(5), 2246-2259. https://doi.org/10.1021/acs.macromol.3c02632

Document license:
CC BY

DOI:
10.1021/acs.macromol.3c02632

Document status and date:
Published: 12/03/2024

Document Version:
Publisher's PDF, also known as Version of Record (includes final page, issue and volume numbers)

Please check the document version of this publication:

• A submitted manuscript is the version of the article upon submission and before peer-review. There can be important differences between the submitted version and the official published version of record. People interested in the research are advised to contact the author for the final version of the publication, or visit the DOI to the publisher's website.
• The final author version and the galley proof are versions of the publication after peer review.
• The final published version features the final layout of the paper including the volume, issue and page numbers.

Link to publication

General rights
Copyright and moral rights for the publications made accessible in the public portal are retained by the authors and/or other copyright owners and it is a condition of accessing publications that users recognise and abide by the legal requirements associated with these rights.

• Users may download and print one copy of any publication from the public portal for the purpose of private study or research.
• You may not further distribute the material or use it for any profit-making activity or commercial gain
• You may freely distribute the URL identifying the publication in the public portal.

If the publication is distributed under the terms of Article 25fa of the Dutch Copyright Act, indicated by the "Taverne" license above, please follow below link for the End User Agreement:

www.tue.nl/taverne

Take down policy
If you believe that this document breaches copyright please contact us at:

openaccess@tue.nl

providing details and we will investigate your claim.

Download date: 07. Jul. 2024

Macromolecules

Open Access

This article is licensed under CC-BY 4.0

pubs.acs.org/Macromolecules

Article

Fiber-Induced Crystallization in Elongational Flows

Paul M. H. van Heugten, Stan F. S. P. Looijmans,* Frank P. A. van Berlo, Martin Rosenthal, Patrick D. Anderson, and Lambèrt C. A. van Breemen*

Cite This: *Macromolecules* 2024, 57, 2246−2259

Read Online

ACCESS | Metrics & More | Article Recommendations | Supporting Information

ABSTRACT: Morphology development at the fiber/matrix interphase in fiber-reinforced isotactic polypropylene composites is a widely studied topic. While the application of shear flow may strongly enhance the nucleation density around the fiber, little is known about the influence of fibers on the crystallization of polypropylene subjected to an extensional flow. In this work, the flow around a single glass fiber upon uniaxial elongation of the melt is examined using X-ray scattering and diffraction techniques and compared to the response measured for the neat matrix. A comparison between a neat and compatibilized matrix is made given the strong influence of the addition of an adhesion modifier on the bulk crystallization kinetics of polypropylene. The flow is applied using an in-house-built filament stretching extensional rheometer, which, due to its midfilament control scheme, allows for in situ X-ray experiments. Combined small-angle X-ray scattering/wide-angle X-ray diffraction patterns are acquired during the flow and subsequent crystallization step. Postcrystallization area scans of the filament show that the introduction of a single glass fiber gives rise to the development of β-phase crystals, particularly in the area around the fiber ends, and in contrast to what is observed for the matrix materials alone, where solely α-phase is found. Surprisingly enough, the addition of a single fiber (0.00045 vol %) alters the crystallizing polymorph in almost the entire filament. However, the addition of the adhesion modifier hinders the formation of β-phase crystals around the fiber due to an acceleration of the bulk crystallization kinetics. Finite element simulations provide insight into the flow field around the fiber during stretching and demonstrate that the flow is no longer uniaxial extension, but dominated by shear, even though the volumetric amount of fiber as compared to the matrix is negligible. These findings explain the experimental observation of substantial β-phase formation after the introduction of a single fiber, while this is not observed in the matrix material. Worth noting, the formation of β-phase polypropylene depends not only on the presence and the strength of the flow but predominantly on the type of flow, i.e., shear as opposed to elongation.

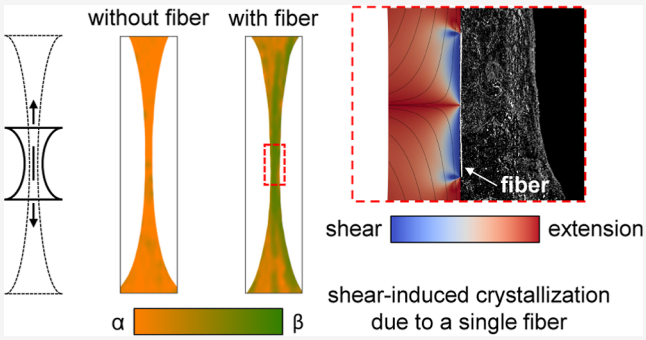

Downloaded via TU EINDHOVEN on March 13, 2024 at 08:33:48 (UTC).
See https://pubs.acs.org/sharingguidelines for options on how to legitimately share published articles.

■ INTRODUCTION

In the production of polymer materials, fibers are often added to improve the performance of the final product.[1] During processing, the material is usually dominated either by shear or extensional flow.[2,3] Generally, an extension flow is a significantly stronger flow type than shear since the separation length between two fluid elements is exponential as opposed to linear in the case of shear flow.[4] When considering one of the most common processing techniques to produce fiber-reinforced composites, i.e., tape extrusion, a strong elongational flow is experienced by the polymer chains between the slit-die and the water-cooled roller. Upon cooling the material, the molecular orientation of the chains is frozen in either by crystallization or by passing through T_g.[5] Implications on the mechanical response of the product, for instance, depend mostly on the strength and modulus of the fiber and polymer matrix,[6,7] the fiber-length and fiber-orientation distribution,[8,9] and stress-transfer efficiency between the fiber and the matrix.[10−12] These are determined, first and foremost, by the morphology of the semicrystalline matrix, which is influenced by the molecular orientation of the polymer chains.[13−15]

Isotactic polypropylene (iPP) is selected as a matrix material for this study as it is often used in both industrial and commercial applications[16] and due to its thermoplastic nature and decent mechanical properties increasingly used in composite materials.[17−20] Its crystallization kinetics and morphology development around fibers are of particular interest to improve the mechanical and physical properties of the composite as a whole.[21,22] Depending on the processing conditions applied, iPP can display a rich polymorphism; the most commonly known crystal modifications are monoclinic α-phase (moderate cooling), trigonal β-phase (temperature

Received: December 21, 2023
Revised: January 26, 2024
Accepted: February 7, 2024
Published: February 27, 2024

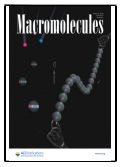

ACS Publications

© 2024 The Authors. Published by American Chemical Society

https://doi.org/10.1021/acs.macromol.3c02632
Macromolecules 2024, 57, 2246−2259

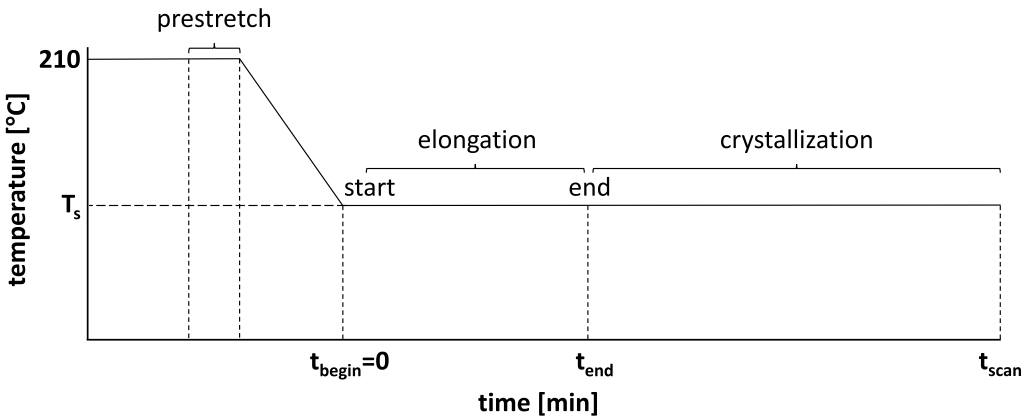

Figure 1. Schematic representation of the experimental procedure. The sample is heated up above its melting temperature T_m to erase any thermal history of the material, after which the filament is given a prestretch. The filament is cooled at the maximum cooling rate to the desired temperature, followed by the isothermal measurement.

gradient and flow), orthorhombic γ-phase (high pressure), and mesophase (rapid cooling) .[23−28]

Besides the complex polymorphism of iPP, its semicrystalline morphology strongly depends on the processing conditions as well.[29−31] With increasing flow strength, the isotropic spherulitic morphology first becomes more refined, i.e., the size of the spherulites reduces, and under strong shear flow conditions becomes a highly anisotropic, often referred to as a "shish-kebab", morphology.[29,30] In the case of polypropylene composites, Varga and Karger-Kocsis[32] have shown that transcrystalline-type microstructures develop around fibers in an iPP matrix. A distinction has to be made between quiescent and shear flow conditions. Under quiescent conditions, a so-called transcrystalline structure develops under the influence of heterogeneous nucleation. Many α-nuclei are present at the surface of the fiber, and as a result, the α-iPP crystals grow perpendicular to the fiber surface. The growth of an α-crystal that develops is restricted in the direction parallel to the fiber due to the growth of neighboring structures.[33]

Under shear flow conditions and isothermal crystallization, a cylindritical structure develops from the melt.[34] The molecular chains become aligned along the fiber direction, and a columnar layer of oriented α-row nuclei is formed. The layer of α-row nuclei gives rise to the cross-nucleation of β-nuclei that covers the surface of the columnar layer. Similar to a transcrystalline structure, the lateral growth of the growing polymorph is restricted. Besides the β−β impingement lines, also a crystal alteration from α- to β-phase occurs, i.e., α−β bifurcation.[35−37] When subsequently an adhesion modifier is added to the neat polypropylene matrix, this transition upon the application of shear flow is inhibited as recently demonstrated.[38] Here, it is shown that under shear flow conditions, an isotropic morphology consisting of extremely small α-spherulites develops for the adhesion-modified polypropylene. The addition of a trace amount of the low-molecular-weight compatibilizer slightly increases the bulk crystallization kinetics under quiescent conditions, an effect which is strongly amplified under shear flow conditions. The faster overall crystallization kinetics due to the larger nucleation density lower the time needed to reach full space-filling and hence hinder the β-phase formation. As a result, a highly refined, isotropic morphology of α-phase spherulites develops. Note that an adhesion modifier[39] is added in combination with a chemically functionalized fiber surface[40] to improve adhesion and stress transfer at the interphase by covalent coupling and/or enhancing secondary non-covalent interactions.

In this work, the influence of adding maleic anhydride-grafted polypropylene as a compatibilizer on the crystallization kinetics of polypropylene in an extensional flow is considered and compared to earlier findings under shear flow conditions.[38] Subsequently, a single fiber is introduced, and a full in situ characterization of its influence on the developed microstructure is performed. By using only a single fiber, the effect of fiber−fiber interactions and edge effects can be inherently excluded from the results in order to gain fundamental insight into the role of a single fiber on the crystallizing morphology. The crystal structure and crystallization kinetics are examined using in and ex situ X-ray scattering techniques. Using a filament stretching rheometer, a uniaxial elongational flow is applied on the samples, while the synchronized motor movement keeps the point of interest in view of the X-ray beam. Optical imaging techniques are used to verify and locate both the position and orientation of the fiber. In addition, they are used both during flow to track the movement of the fiber and after flow to follow the crystallization of the stretched sample. To explain the strong influence of adding solely a single fiber to the sample (0.00045 vol %) on the crystallizing polymorph, finite element simulations are performed to visualize the flow field around a fiber in the center of the filament during uniaxial stretching. It could be demonstrated that the presence of a single fiber (or another impurity) is sufficient to convert an extensional flow profile into a shear flow, and that this effect is not limited to the interphase but manifests itself in a large fraction of the sample.

■ EXPERIMENTAL METHODS

Materials and Sample Preparation. In this study, an injection molding grade iPP with a weight-average molecular weight of 365 kg/mol and a polydispersity index of 5.5 is kindly provided by Borealis Polyolefine GmbH (Linz, Austria). As a compatibilizer, 5% of a maleic anhydride-grafted polypropylene (MAH-*g*-PP) from Exxon (PO1020), with a grafting content of up to 1%, is melt-blended into the, respective, homopolymer using a ThermoElectron Rheomex OS − PTW 16 twin-screw extruder, kindly provided by PTG/e, with corotating screws (length/diameter = 40). A detailed preparation procedure of these materials, molar mass distribution, and full relaxation spectrum are described in our previous work.[38] The single

https://doi.org/10.1021/acs.macromol.3c02632
Macromolecules 2024, 57, 2246−2259

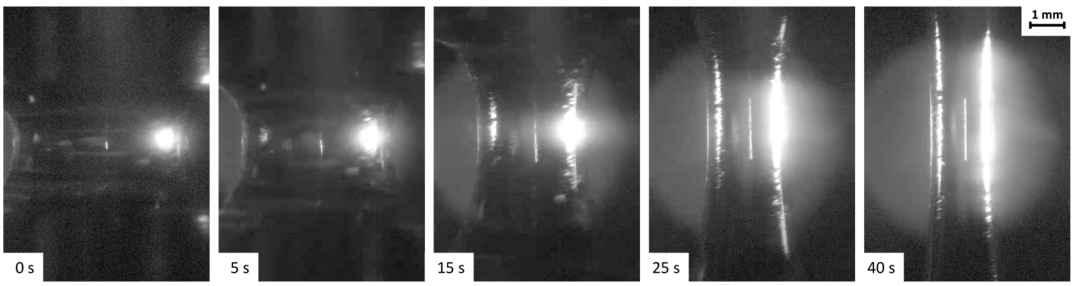

Figure 2. Photographs during various stages of the elongation in chronological order from left to right. The filament consists of an iPP matrix containing a single glass fiber elongated at a strain rate of 0.05 s^{-1} until a true strain of 2. The bright spot is caused by the laser, which measures the diameter of the filament.

glass fiber samples are prepared using a continuous glass fiber with a diameter of 17 μm and a silane coupling agent (Nippon Electric Glass, Otsu, Japan).

From the raw granulate materials, plates with dimensions of 200 × 200 × 2 mm^3 are compression molded using a Fontijne Holland (TP 400) hot press. The polymer is sandwiched between steel plates of 1 mm thickness coated with polytetrafluoroethylene sheets of 0.5 mm thickness to prevent sticking of the compatibilized material, subsequently molten at 230 °C and compressed for 3 min at a force of 100 kN. After that, the stack is quenched to a temperature of 20 °C in the cold part of the press. For the neat and compatibilized samples, disks with a diameter of 8 mm are punched from the compression molded plates.

To prepare a single, sized glass fiber (SGF) specimen, a hole has been punctured in the center of an iPP disk. Successively, a single glass fiber with a length of 5 mm is placed in the punctured hole. The polymer disk is then gradually heated to 200 °C such that the polymer matrix fully encapsulates the fiber and no air pockets are present. After the molten polymer surrounds the fiber, it is ensured that the fiber is placed straight, i.e., vertically and coaxially aligned, into the punctured hole. Subsequently, the fiber is pressed down such that it reaches both parallel surfaces of the molten polymer disk. After the sample is cooled down gradually, the part of the fiber which is not encapsulated is cut off.

Experimental Procedure. The experimental setup used is an in-house-built filament-stretching extensional rheometer (FiSER).[41] The design of the FiSER concurrently allows for measuring the rheological response and performing in situ X-ray experiments during elongation since the center of the filament remains at a constant position in the FiSER. A constant strain rate is applied by means of a closed-loop control scheme for the rotation speed of the bottom and top pistons, which simultaneously move apart.[42]

The two plates of the FiSER are heated to 210 °C before the sample is placed. The polymer disk is then placed and molten to erase its thermomechanical history. Consecutively, the sample is compressed to obtain proper contact with both plates and attain a cylindrical shape, whereafter the sample is prestretched to create a concave shape. Hereafter, the experimental protocol, as visualized in Figure 1, is followed; first, the sample is cooled at a rate of 5 °C/min, which is the maximum cooling rate of the device, to the desired stretching temperature. The smallest diameter of the concave sample, measured by a laser micrometer as explained in more detail in ref 41, is controlled during the experiment to attain a constant Henky strain rate. By doing so, in the center of the filament, a uniaxial elongational flow is applied at a constant strain rate of 1 s^{-1} until a true strain of 3 is reached. Throughout the experiment, the temperature is kept constant, and preheated nitrogen gas is flushed to ensure a homogeneous temperature of the entire sample and prevent oxidative degradation of the matrix material.

A monochrome camera (Pixelink PL-D775MU-T) equipped with a 55 mm f/2.8 Nikon micro-Nikkor lens is used to take optical images at a rate of 30 frames per second. By observing changes in the opacity of the sample, the time scale of the crystallization process is estimated. Moreover, these recordings prove that the fiber which is introduced remains in the center of the filament during stretching. It is shown in Figure 2 that upon pulling, the fiber remains straight and that a slight crystallization around the fiber is already present. Nonetheless, it is necessary to mention that although the fiber remains centered in the filament during stretching, it sags significantly after stretching, due to the relatively slow crystallization of the nonstretched part of the sample.

Computed Tomography Scans. To verify the location of the single fiber after the stretching experiment, two-dimensional X-ray computed tomography images are acquired on a Nanotom 160NF Phoenix (General Electric, Boston, Massachusetts, USA). Images with a pixel size of 2.000 μm are acquired using an accelerating voltage of 60 keV and a beam current of 310 μA. The exposure time is set to 1000 ms, and an average of six exposures is presented.

Beamline Setup. In situ and ex situ small-angle X-ray scattering (SAXS) and wide-angle X-ray diffraction (WAXD) experiments have been performed at the European Synchrotron Radiation Facility (ESRF) in Grenoble, France. The Dutch-Belgian Beamline (DUBBLE), BM26, is used with the combined SAXS/WAXD setup.[43] The alignment of the FiSER to the incoming X-ray beam is performed analogous to that of Pepe et al.,[41] where an X-ray transmission scan is performed in the x- and z-direction to locate the midfilament point. By assuming cylindrical symmetry of the sample, this point should coincide with the smallest diameter measured by the laser micrometer in the direction perpendicular to the X-ray beam.

A Pilatus 1M detector (981 × 1043 pixels and a pixel size of 172 × 172 μm^2) and a quasi-linear 300K−W Pilatus detector (1475 × 195 pixels and a pixel size of 172 × 172 μm^2) have been used for the combined SAXS and WAXD measurements, respectively. The SAXS and WAXD detectors are placed at a direct distance from the sample of 3.451 and 0.308 m, respectively. A wavelength of 1.0332 Å and a beam size of 300 × 400 μm^2 are used.

The distance and tilt angle calibration is done using Al_2O_3 (aluminum oxide) for the WAXD detector and AgBE (silver behenate) for the SAXS detector. The acquisition protocol applied for the in situ measurements is given in Table 1. The protocol is developed using the relevant time scales obtained for the optical images and lasts approximately 1 h. The number of frames and the exposure times are varied depending on the expected crystallization behavior of each sample.

Postprocessing of the X-ray Data. The collected data is analyzed using the software program FIT2D, developed by the ESRF.[44−46] A mask is applied to the data to exclude the pixel regions

Table 1. Acquisition Protocol of the In Situ X-ray Experiments during Which the Filament Is Elongated and Subsequently Completely Crystallized

	exposure time [s]	delay [s]	number of frames [-]
step 1	1	0	120
step 2	5	0	12
step 3	5	25	20
step 4	5	55	48

https://doi.org/10.1021/acs.macromol.3c02632
Macromolecules 2024, 57, 2246−2259

of the beam stop and gaps of the detector. The measured intensity I_m and the air-scattering background I_{bkg} are normalized by the incident flux I_1 and the background incident flux $I_{1,bkg}$, respectively. A correction factor C for the absorption factor and varying flux is given by[47]

$$C = \frac{I_{1,bkg} \cdot I_2}{I_{2,bkg} \cdot I_1} \tag{1}$$

where I_2 is transmitted beam intensity during the experiment and $I_{2,bkg}$ is the transmitted beam intensity of the background. The transmitted intensity is measured by the photodiode placed in the beam stop. As the diameter of the filament decreases over time, the measured intensity needs to be corrected for the decrease in sample thickness d_t, given by the following expression[48]

$$d_t = \mu \cdot \ln\left(\frac{I_{2,bkg} \cdot I_1}{I_{1,bkg} \cdot I_2}\right) \tag{2}$$

where μ is the absorption factor, which is assumed to be constant throughout the experiment and therefore not taken into account, i.e., set equal to 1, as this is simply a vertical scaling of an already arbitrary intensity. The decreasing thickness leads to an increase in transmission Tr given by[48]

$$Tr = \frac{I_{2,bkg} \cdot I_1}{I_{1,bkg} \cdot I_2} \tag{3}$$

The corrected intensity I_{corr} is given by the following equation[48,49]

$$I_{corr} = \frac{\left(\frac{I_m}{I_1} - C \cdot \frac{I_{bkg}}{I_{1,bkg}}\right)}{Tr \cdot d_t} \tag{4}$$

The α- and β-polymorphs of iPP are distinguished using the corrected intensity of the integrated WAXD pattern. Therefore, Lorentz curves are fitted to the intensity peaks of their $(130)_\alpha$ and $(300)_\beta$ lattice planes, respectively. An example is given in Figure 3,

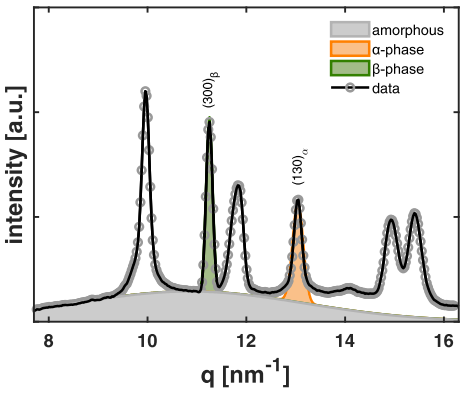

Figure 3. An example is presented of the corrected, integrated WAXD pattern of iPP with a single glass fiber measured at a temperature of 133 °C after complete crystallization of the filament, represented by the black line and open gray markers. The amorphous halo is fitted first, represented by the gray-colored area, after which the crystalline peaks for α- and β-iPP are fitted, indexed, and colored by the orange and green areas, respectively. The sample is elongated to a true strain of 3 at a strain rate of 1 s^{-1}.

where the fitting of the amorphous halo is indicated as well. This halo was determined from the first frame, i.e., the supercooled melt at the isothermal crystallization temperature. The areas under the deconvoluted diffraction peaks are used to determine the weight fraction of crystallinity χ_w

$$\chi_w = \frac{A_{total} - A_{amorph.}}{A_{total}} \tag{5}$$

where A_{total} is the integrated area of the corrected intensity and $A_{amorph.}$ is the area under the fitted amorphous halo. The deconvoluted area beneath the characteristic α- and β-reflections is used to determine the relative crystal phase content $\chi_{r,i}$, which is given by[26]

$$\chi_{r,i} = \frac{A_i}{A_\alpha + A_\beta} \tag{6}$$

where A_α and A_β are related to the corresponding α- and β-intensity peaks, respectively. The areas for γ- and mesophase have not been taken into account due to the negligibly small presence of these polymorphs.

NUMERICAL MODELING

Problem Description. The flow field around a single fiber is investigated using a Newtonian fluid model. The axisymmetric finite element model according to van Berlo et al.[50] is used to describe the fluid motion and stresses in a FiSER. The geometry is adapted for the problem to include a single inclusion. The balance of momentum and mass is given by the following equations

$$\rho \frac{D\boldsymbol{u}}{Dt} = -\nabla p + \nabla \cdot \boldsymbol{\tau} + \rho g \boldsymbol{e}_g \text{ in } \Omega,$$
$$\nabla \cdot \boldsymbol{u} = 0 \text{ in } \Omega. \tag{7}$$

Here, ρ is the fluid density, p is the pressure, $\boldsymbol{u}$ is the fluid velocity, $\boldsymbol{\tau}$ is the extra stress tensor, and g is the gravitational acceleration. The fluid is assumed to be incompressible. A Newtonian constitutive equation is used, where the extra stress tensor is expressed as[4]

$$\boldsymbol{\tau} = 2\eta \boldsymbol{D} \tag{8}$$

where η is the shear viscosity and $\boldsymbol{D}$ is the deformation-rate tensor. The material, rheological, and experimental parameters used for the simulation are given in Table 2. Here, the viscosity

Table 2. Material, Rheological, and Experimental Parameters Used for the Finite Element Simulation at a Temperature of 133 °C[13]

material	η [Pa s]	ρ [kg/m^3]	$\hat{\gamma}$ [mN/m]	$\dot{\varepsilon}$ [s^{-1}]	ε [-]
iPP	6725	800	30.2	1	3

is obtained by taking the shear viscosity at an effective shear rate of $\sqrt{3}\dot{\varepsilon}$ for the iPP_1[13] material used in the work of Roozemond et al.[13] at a temperature of 160 °C.[51] The obtained value is then shifted to a temperature of 133 °C using the Arrhenius equation.[52]

The work of van Berlo et al.[50,51] is followed for applying the mesh movement and remeshing and projection procedure in the numerical simulation.[53−55] Here, a detailed explanation of the finite element model can be found. Analogously, the controller of the radius, which is added to ensure the radius decreases exponentially such that the strain rate is constant, is adopted from the work of Román Marín et al.[42] The domain Ω is discretized using triangular, isoparametric, P_2−P_1 (Taylor-Hood) elements for the interpolation of the velocity and pressure. The model is simulated using the in-house built finite element software package TFEM.

Geometry and Boundary Conditions. The geometry of the FiSER containing a single inclusion is presented in Figure

https://doi.org/10.1021/acs.macromol.3c02632
Macromolecules 2024, 57, 2246−2259

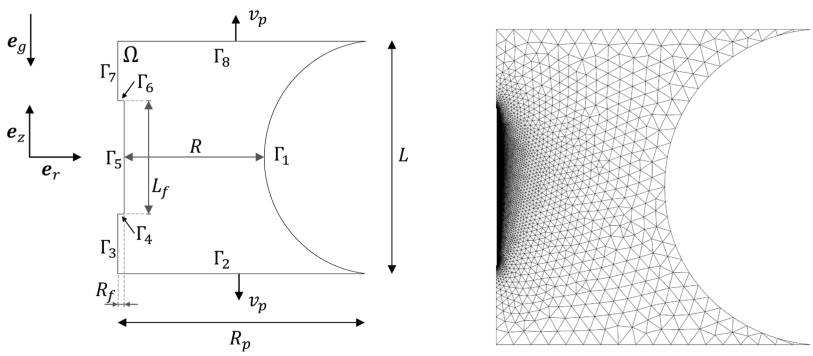

(a) (b)

Figure 4. (a) Graphical representation of the geometry with an inclusion aligned to the flow direction in a FiSER. The free surface is described by Γ_1, and the bottom and top pistons are described by Γ_2 and Γ_8, respectively, which move with a velocity v_p in the opposite direction. The axisymmetric boundary is given by Γ_3 and Γ_7. Furthermore, the inclusion is described by Γ_4, Γ_5, and Γ_6. (b) Finite element mesh consisting of triangular elements, with a mesh refinement toward the fiber ends, generated using Gmsh.[54]

4a. Initially, the geometry is built using Gmsh,[54] as is shown in Figure 4b. The shape of the filament is determined by the representative dimensions of the experiment and given as the initial midfilament radius R_0 of 2.2 mm, the radius of fluid at the pistons R_p of 4 mm, and the initial length of the filament L_0 of 3.88 mm. It is assumed that the inclusion, described by boundaries Γ_4, Γ_5, and Γ_6, remains stationary during the simulation as the mass ratio $m_{\text{fiber}}/m_{\text{matrix}}$ is approximately equal to 2×10^{-5}. Two limiting cases are considered, one where there is a perfect adhesion between the matrix material and the inclusion (no-slip) and one where this interaction is absent (full slip). The inclusion is represented with a length L_f of 2 mm and a radius R_f of 8.5 μm. A cylindrical coordinate system is used with the components $[r, \theta, z]$.

The bottom and top pistons are described by curve Γ_2 and Γ_8, respectively. The pistons move with a controlled velocity v_p in the opposite direction, and a no-slip condition is assumed at the piston boundary. Therefore, the following boundary conditions are prescribed on the pistons

$$u_r = 0 \text{ on } \Gamma_2 \text{ and } \Gamma_8$$
$$u_z = -v_p \text{ on } \Gamma_2$$
$$u_z = v_p \text{ on } \Gamma_8 \tag{9}$$

On the symmetry line, the velocity in the radial direction is prescribed

$$u_r = 0 \text{ on } \Gamma_3 \text{ and } \Gamma_7 \tag{10}$$

The velocity component normal to the fiber curves is prescribed to be zero because the fluid cannot flow inside the fiber. So, in combination with the no-slip condition, the boundary condition is

$$\boldsymbol{u} = \boldsymbol{0} \text{ on } \Gamma_4, \Gamma_5, \text{ and } \Gamma_6 \tag{11}$$

However, for a full-slip condition, the tangential velocity component equals the flow velocity and the boundary condition reduces to

$$\boldsymbol{u}\cdot\boldsymbol{n} = 0 \text{ on } \Gamma_4, \Gamma_5, \text{ and } \Gamma_6 \tag{12}$$

where $\boldsymbol{n}$ is the normal outward to the surface. The surface tension acting on boundary Γ_1 is imposed by the following definition

$$(-p\boldsymbol{I} + \boldsymbol{\tau})\cdot\boldsymbol{n} = \nabla_s\cdot(\hat{\gamma}(\boldsymbol{I} - \boldsymbol{nn})) \text{ on } \Gamma_1 \tag{13}$$

where $\hat{\gamma}$ is the surface tension coefficient and ∇_s is the surface gradient operator.

Postprocessing. A frame-indifferent criterion to distinguish flow types is the dimensionless non-negative persistence-of-straining parameter $\mathcal{R}$, which is given by[56,57]

$$\mathcal{R} = \frac{\sqrt{\frac{1}{2}\text{tr}(\boldsymbol{P}^2)}}{\text{tr}(\boldsymbol{D}^2)} \tag{14}$$

where $\boldsymbol{P}$ is the persistence-of-straining tensor computed according to Park.[56]

To contrast areas that exhibit shear or elongational flows, the dimensionless flow-classification parameter ϑ is used, which is given by the following definition[58]

$$\vartheta = \frac{1 - \mathcal{R}}{1 + \mathcal{R}} \tag{15}$$

Here, the values of ϑ are linked to the flow type as the following[58]

$$\vartheta = \begin{cases} 1 & \text{extension} \\ 0 & \text{shear} \\ -1 & \text{rigid body motion} \end{cases} \tag{16}$$

where rigid body motion is related to the flow being stationary or translated without rotation, when the computed persistence-of-straining parameter approaches infinity ($\mathcal{R} \to \infty$).

■ RESULTS AND DISCUSSION

Crystallization Kinetics and Phase Composition. The rheological response of iPP, iPP with 5% MAH-*g*-PP, iPP with a single glass fiber, and iPP with 5% MAH-*g*-PP and a single glass fiber is measured concurrently with the X-ray scattering experiments during the elongation of the filaments.[41] However, due to the relatively low zero shear viscosity of the iPP matrix,[38,59] the rapid decrease in filament diameter upon uniaxial stretching, and the lack of strain hardening in iPP, the recorded force signal decreases to its sensor noise value within 1 s, and no reliable extensional viscosity could be obtained. Therefore, the rheological response of these materials in extension is not discussed further in the remainder of this work. The lowest attainable stretching temperature with no quiescent crystallization upon cooling (133 °C) is used as the low viscosity leads to extreme sagging of the material due to

https://doi.org/10.1021/acs.macromol.3c02632
Macromolecules 2024, 57, 2246−2259

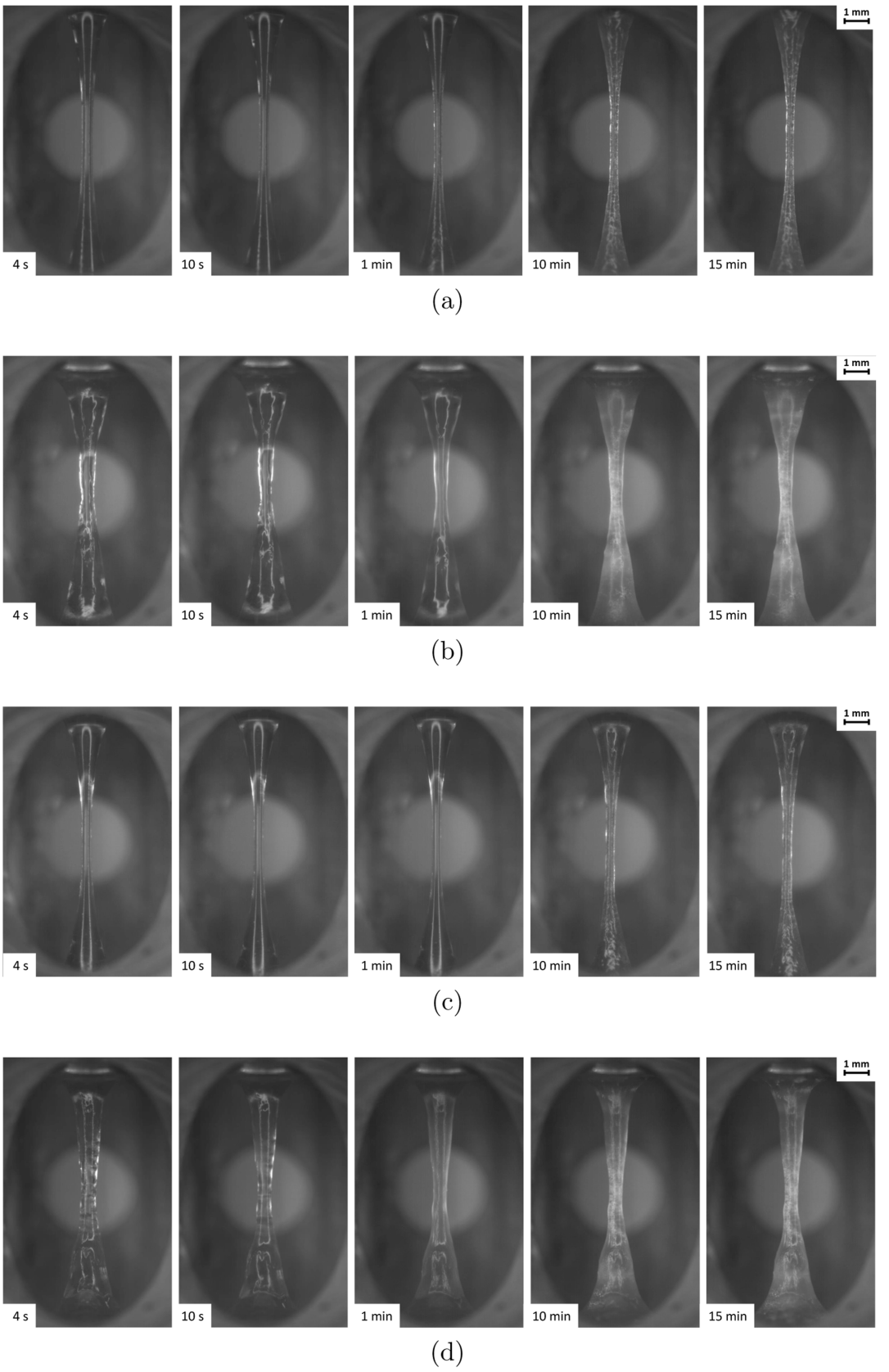

Figure 5. Photographs of (a) iPP, (b) with 5% MAH-*g*-PP, (c) with an SGF, and (d) with 5% MAH-*g*-PP and an SGF sample in chronological order from left to right, where the time of the photograph after beginning the elongation is indicated. For all cases, the filaments are elongated at a strain rate of 1 s^{-1} until a true strain of 3, after which the samples are let to crystallize isothermally at a temperature of 133 °C.

https://doi.org/10.1021/acs.macromol.3c02632
Macromolecules 2024, 57, 2246−2259

Table 3. Comparison of the Avrami Fit on the In Situ WAXD Data of iPP, iPP with MAH-*g*-PP, and iPP with a Single Glass Fiber[a]

material	iPP	+ 5% MAH-*g*-PP	+ SGF	+ 5% MAH-*g*-PP + SGF
N	2.702 ± 0.080	2.038 ± 0.031	2.667 ± 0.135	2.182 ± 0.038
K [min^{-1}]	0.040 ± 0.007	2.730 ± 0.070	0.138 ± 0.035	4.012 ± 0.095
t_0 [s]	60	0.1	30	0.1
$t_{1/2}$ [min]	13.02	3.8	8.49	2.92

[a]The samples are elongated to a true strain of 3 at a strain rate of 1 s^{-1} and a temperature of 133 °C.

gravity after the stretching step and before crystallization sets in. The temperature is rather high compared to earlier studies[38] due to the low cooling rate of the FiSER.[41] As a result, filament breakup is easily observed at high strains and/or low strain rates.

The addition of the MAH-*g*-PP compatibilizer to iPP slightly lowers the zero-shear viscosity as has been demonstrated before.[59] The material has initially less resistance to flow, which results in a slightly more homogeneous neck distribution. The deformed shapes of the neat and compatibilized filaments are shown in Figure 5. Upon stagnation of the flow, the necking of both samples is almost equal. However, the presented time-lapse of the crystallization after the filament has been stretched shows a substantial difference. The neck dimensions of MAH-*g*-PP-compatibilized iPP remain unaltered, while there is a significant size reduction of the midfilament diameter in neat iPP. In addition, the change in opacity of the sample indicates a faster crystallization process in the compatibilized sample. Both these findings are in line with earlier results obtained for these materials under shear flow conditions[38] and may be explained in a similar manner; the addition of MAH-*g*-PP gives rise to the abundant nucleation of small spherulites which lead to rapid stabilization of the filament shape and enhanced crystallization kinetics. On the contrary, the neat iPP sample crystallizes slower, which leads to a stronger influence of gravity and surface tension on the midfilament diameter, and the lower number of nuclei causes larger spherulitic superstructures to be formed (as is apparent from Figure 5b). The influence of adding a single glass fiber to both neat iPP and compatibilized iPP is marginal. A slight increase in the filament length can be observed, which can be explained by an additional shear component along the fiber, causing an additional extension during the elongation of the filament, as the midfilament diameter and not the length of the filament is controlled via a comprehensive control scheme.[41]

To quantify the apparent difference in crystallization time scale, unravel the phase composition, and understand the developed morphology, in situ X-ray diffraction and scattering experiments have been performed at the DUBBLE BM26 beamline,[43] part of the ESRF, Grenoble, France. Four samples are considered, namely, neat iPP, compatibilized iPP with 5% MAH-*g*-PP, neat iPP with a single glass fiber, and compatibilized iPP with 5% MAH-*g*-PP and a single glass fiber. The weight fraction crystallinity is determined from quasi-1D WAXD data recorded during filament stretching and subsequent crystallization at a temperature of 133 °C. Although the difference in crystallinity between the samples is found to be small, the relative, i.e., normalized, crystallinity χ_c is considered here and described by means of the Avrami equation[60−62]

$$\chi_c = 1 - \exp\left(-K(t - t_0)^n\right) \tag{17}$$

where t is the time, t_0 is the onset of crystallization, n is the Avrami exponent, and K is the overall crystallization rate constant.[63] The Avrami equation has been fitted to the relative crystallinity data, as shown in Figure 6. The weight fraction of crystallinity over time is determined according to eq 5 and scaled with the final crystallinity.

A first-order polynomial is fitted, using a nonlinear-least-squares method, to the relative crystallinity data plotted as ln $(-\ln(1 - \chi_c))$ versus ln $(t - t_0)$. The slope and intercept then correspond to the parameters n and K, respectively, and the resultant curve is shifted to determine the onset time of crystallization. Table 3 presents the fitted values for the three different samples, including the crystallization halftime $t_{1/2}$, which is given by[64]

$$t_{1/2} = \frac{\ln(2)^{1/n}}{K^{1/n}} \tag{18}$$

The observation of the faster crystallization kinetics by optical examination is confirmed by the results from the WAXD experiments presented in Figure 6 and the fitted

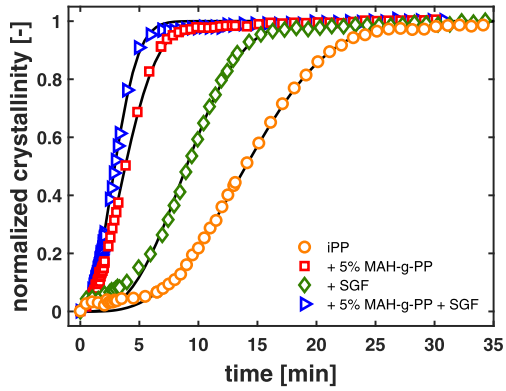

Figure 6. Measured relative crystallinity χ_c (symbols) and the fitted Avrami equation (line) are presented over time for iPP, iPP with 5% MAH-*g*-PP, iPP with a single glass fiber, and iPP with 5% MAH-*g*-PP and a single glass fiber. The samples are elongated to a true strain of 3 at a strain rate of 1 s^{-1} and a temperature of 133 °C.

Avrami parameters derived from that. The onset of crystallization t_0 for an iPP matrix occurs only after the stagnation of the extensional flow. The addition of MAH-*g*-PP results in a distinctly earlier onset of crystallization, possibly already during flow, and results in a higher rate parameter K, lower crystallization halftime $t_{1/2}$, and two-dimensional growth instead of three-dimensional growth of the crystals based on the Avrami exponent n. The optical appearance of the samples suggests that the nucleation density of the compatibilized iPP is higher than that of neat iPP. As discussed above, the earlier onset of crystallization and higher nucleation density prevent material from sagging and stabilize the shape of the filament.

https://doi.org/10.1021/acs.macromol.3c02632
Macromolecules 2024, 57, 2246−2259

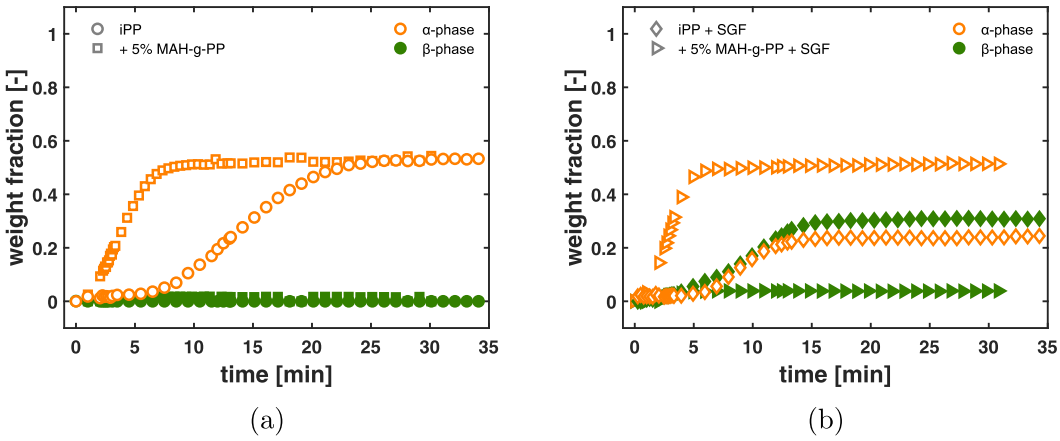

Figure 7. Weight fraction evolution measured via in situ WAXD during isothermal elongation at a constant strain rate of 1 s^{-1} to a true strain of 3 and subsequent isothermal crystallization at a temperature of 133 °C. The presented samples are (a) iPP and iPP with 5% MAH-*g*-PP, (b) iPP with a single glass fiber, and iPP with 5% MAH-*g*-PP and a single glass fiber.

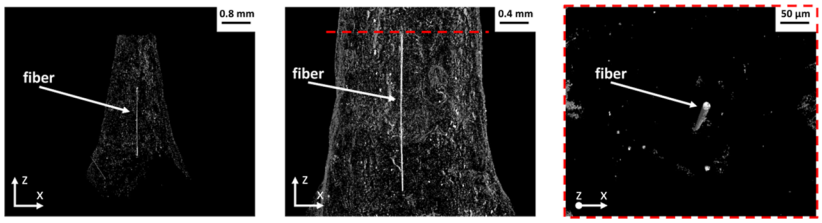

Figure 8. Two-dimensional CT-scan of a fully crystallized iPP filament containing a single glass fiber, which can be recognized by the straight white line. The left-hand side figure shows the bottom half of the filament. The center figure presents a zoom-in onto the glass fiber, and in the right-hand side figure, a top view is presented. The used voxel size is 2.000 μm^3.

On the other hand, the difference between iPP and iPP + SGF is marginal. Adding a fiber appears to result in an earlier onset of crystallization and slightly faster kinetics. However, the differences are minute and most probably due to experimental deviations. The overall crystallization rate constant is lower for iPP than for iPP with an SGF; nonetheless, this parameter might be subjected to a larger uncertainty due to the sagging of the fiber. The shift causes the measurement point to move upward along the fiber surface and can therefore not be directly related to a constant value around the midfiber point.

In addition to the normalized relative crystallinity, the relative weight fraction development between α- and β-iPP is examined using the recorded in situ quasi-1D WAXD data. For neat iPP, a distinct development of α-phase can be observed, as depicted in Figure 7a. Analogous to what is observed in shear flow,[38] the addition of the compatibilizer results in a faster overall crystallization time, yet in extension, contrary to shear, it does not change the developed crystal phase nor does it influence the total crystallinity. It must be recalled that the absolute crystallinity cannot be determined due to the quasi-1D WAXD detector in the combined SAXS/WAXD setup.

In the case that a single glass fiber is added to a neat iPP matrix, an abundant development of β-phase under elongational flow conditions is observed (Figure 7b). A considerable amount of β-iPP is formed due to the alignment of small-scale-oriented α-crystals on which β-iPP crystals can form and grow.[32] Similar to shear flow conditions,[38] the development of β-phase is not shown in the compatibilized iPP. The formation of β-iPP crystals is suppressed due to the plentiful nucleation of α-phase crystals which also leads to significantly faster crystallization kinetics.

To verify that the development of β-phase in the neat iPP matrix is due to the presence of the fiber rather than an artifact of the sample preparation method, additional experiments are performed where a sample is produced the same as the single fiber sample but without adding the fiber in the punched hole. The experiments are carried out under isothermal quiescent conditions and extensional flow conditions. The results can be found in the Supporting Information and show that the fiber does not introduce the development of β-phase crystals under quiescent conditions and the punched and remolten hole does not explain the abundant development of β-iPP upon applying an elongational flow. The development of β-crystals is thus due to the flow around the fiber.

After complete crystallization of the filament, the samples are taken from the FiSER, and a two-dimensional computed tomography scan (CT-scan) is made from a filament containing an SGF and presented in Figure 8. The fiber is recognizable by the white vertical line highlighted on the left-hand side. The orientation of the fiber can best be seen in the zoom displayed in the center and on the right-hand side of the figure. The CT-scan of the iPP + 5% MAH-*g*-PP + SGF sample can be found in the Supporting Information. The CT-scans confirm that the fiber remains centered and aligned with the central axis of the midfilament. However, the fiber does not remain at the midfilament point. Along with the matrix material, the fiber sags toward the bottom plate after the elongation halts. After complete crystallization, the fiber may have shifted over a distance more than twice its length. However, as is discussed in the following, this sagging appears to have little effect on the crystallizing morphology as the secondary flow that it introduces proceeds at an extremely low rate with respect to the longest relaxation time of the material.

https://doi.org/10.1021/acs.macromol.3c02632
Macromolecules 2024, 57, 2246−2259

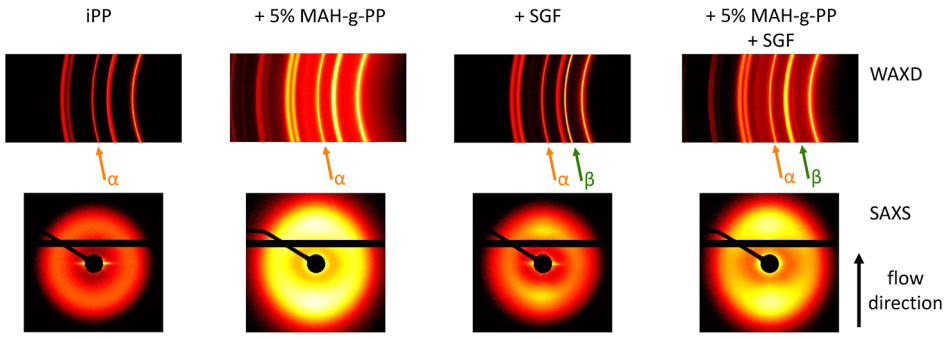

Figure 9. Final frame, where crystallization has finished, of the in situ WAXD (top) and SAXS (bottom) patterns. The samples from left to right are iPP, iPP with 5% MAH-*g*-PP, iPP with a single glass fiber, and iPP with 5% MAH-*g*-PP and a single glass fiber. The filaments are stretched to a true strain of 3 at a strain rate of 1 s^{-1} at a temperature of 133 °C. The measurement is performed at the midfilament point.

The structural and morphological differences between the iPP, iPP with a compatibilizer, iPP with a glass fiber, and iPP with a compatibilizer and glass fiber can be best appreciated by considering the 2D-SAXS and quasi-1D WAXD patterns, as presented in Figure 9. The microstructure of the iPP filament is, in contrary to a shear flow of similar strength,[38] isotropic. The late onset of crystallization gives the polymer molecules sufficient time to relax so that no oriented shish-kebab[30] is formed. In this observation may also lie the explanation for the lack of β-phase formation; the presence of an oriented α-phase layer of crystals is a necessary yet not sufficient condition for the nucleation of β-phase from the bulk, as suggested by Varga.[32] As the applied flow conditions are not able to orient the polymer melt to the extent where oriented α-iPP is able to form, subsequently, the formation of β-phase is inhibited. In this case, the α-crystals are solely faintly oriented to the flow direction and hence cannot give rise to the formation of β-iPP. The apparent shish, shown in the 2D-SAXS figure, is derived from the scattering of the filament edges as the diameter of the filament approaches the horizontal size of the X-ray beam.

Plainly, the sample iPP with MAH-*g*-PP contains the largest amount of lamellar orientation. This is in contrary to earlier findings in the case of shear flow,[38] where compatibilization of the sample led to a decrease in orientation at the lamellar level. Here, the presence of orientation is due to the early onset of crystallization. As a result, the crystals that form during the elongation of the filament orient to the flow direction. However, it is believed that the abundant nucleation density fills the available space rapidly and therewith inhibits the formation of β-phase polypropylene.

In the case of adding an SGF, the presence of orientation is not apparent since the fiber has shifted with respect to the steady measuring position during the in situ X-ray experiments. Nevertheless, the shift downward has not influenced the presence of β-phase at the measuring position. Looking at the quasi-1D WAXD pattern of Figure 9, a strong presence of β-phase is visible. The orientation of this β-phase is not clearly observed. However, a slight indication of orientation for α-iPP can be seen, where the crystals orient themselves parallel to the flow direction. The addition of the compatibilizer to an SGF sample results in the highest observable orientation perpendicular to the flow direction on the lamellar level. A negligible amount of oriented β-phase is observed due to the size of the beam, which is considered to be present toward the edges of the filament, where a slight shear component may be present.

The relative crystal phase content for the four samples under consideration is compared in Figure 10. Here, a two-dimensional X-ray scan in the combined SAXS/WAXD setup is performed over the fully crystallized filaments, i.e., after the previously described elongation experiment is finished. Visualization of the filament is done by measuring the diameter over the length of the filament using the laser micrometer of the FiSER setup, assuming cylindrical symmetry along the central axis of the filament. For iPP, iPP + 5% MAH-*g*-PP, and iPP + 5% MAH-*g*-PP + SGF, the dominant polymorph is α-phase. The formation of small amounts of β-phase is present toward the edges of the iPP filament since a slight shear component may be present at the edges.[65,66]

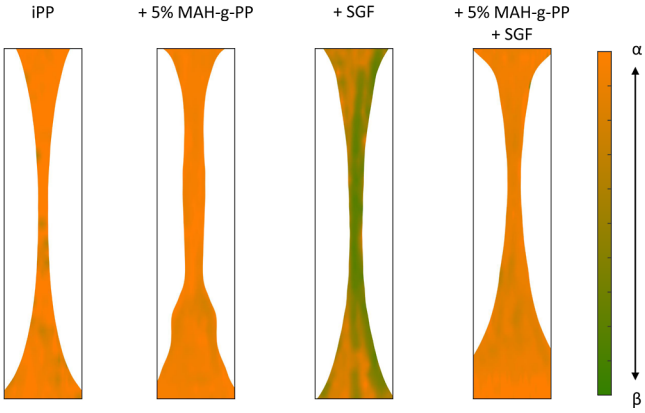

Figure 10. Visualization of two-dimensional scan where the relative α- and β-phase content is presented after stretching and complete crystallization. The samples from left to right are neat iPP, iPP with 5% MAH-*g*-PP, iPP with a single glass fiber, and iPP with 5% MAH-*g*-PP and a single glass fiber. The filaments are stretched to a true strain of 3 at a strain rate of 1 s^{-1} at a temperature of 133 °C. The ex situ scan is performed at a temperature of 20 °C. In the stretching direction, line scans are made every 0.5 mm, containing 42 points each equally distributed over a width of 4 mm, i.e., a stepsize of 0.1 mm.

The introduction of an SGF in a uniaxial elongational flow has a substantial effect on the crystal formation in the bulk. In almost the entire filament, a substantial amount of β-phase has crystallized. This is an utmost remarkable finding as the total volume fraction of the fiber can be calculated to be solely 0.00045%. To evaluate the origin of this peculiar observation, the interphase between the fiber and matrix is examined in more detail in the following.

Crystallization around a Single Fiber. Parallel to the flow direction, a high-resolution analysis is performed directly around an SGF in an iPP matrix. A one-dimensional, vertical

https://doi.org/10.1021/acs.macromol.3c02632
Macromolecules 2024, 57, 2246−2259

line scan is performed over the central axis of the filament using the combined SAXS/WAXS setup, after complete crystallization. In Figure 11, the two-dimensional patterns are shown at three different positions on the fiber, namely, at both the top fiber end, the bottom fiber end, and the midpoint of the fiber. The presence of the fiber (or the oriented structure that is left after sagging) is indicated and can be observed by the horizontal streak of high intensity on the left- and right-hand sides of the beam stop. A slight increase in orientation can be seen in the SAXS patterns when comparing the central location with those of the top and the bottom. The crystals are oriented perpendicular to the fiber and hence, according to the nucleation mechanism proposed by Varga and Karger-Kocsis,[32] could be ascribed to the β-phase crystals that are present as can be seen from the WAXD data. A difference between the center and the top/bottom WAXD patterns is the evident appearance of the $(300)_\beta$-reflection for β-iPP at the fiber tips.

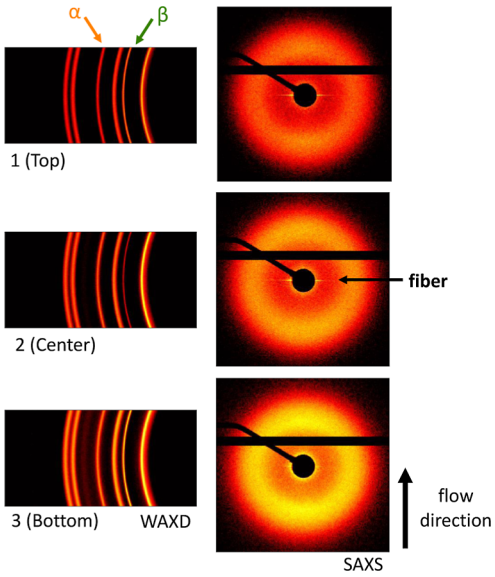

Figure 11. Ex situ WAXD (left) and SAXS (right) patterns of a one-dimensional scan in the z-direction. The presented results of the scan are three measurement points, namely, the top, center, and bottom with respect to the center of the single glass fiber in a neat iPP matrix. The recognition of the fiber is designated by the black arrow. The samples are elongated to a true strain of 3 at a strain rate of 1 s^{-1} and a temperature of 133 °C.

The integrated and corrected WAXD patterns of the three positions around the SGF are presented in Figure 12a. As could have already been deduced from the quasi-1D WAXD patterns, at the center of the filament, the presence of β-phase is minute, while toward the fiber tips, up to 60% of this modification may be found. Another fact shown by the integrated WAXD and SAXS patterns is the symmetry between the top and bottom (Figure 12b). The 2D-SAXS and quasi-1D WAXD patterns and the integrated and corrected WAXD patterns of the three positions, and the one-dimensional line scan around the SGF in a compatibilized iPP matrix can be found in the Supporting Information.

The before-noted symmetry is observed in more detail for a second measured sample, as visualized in Figure 13a. Again, the relative phase content is measured in a one-dimensional line scan along the approximately 2 mm long fiber. The relative crystal phase content around the fiber is approximately symmetric around the mid-fiber point. The fractions $\chi_{r,\beta}$, for instance, at the top and bottom position are 0.31 and 0.32, respectively. This is a clear indication that the structure is formed due to the fiber being present in the initial elongational flow, instead of being an effect of the fiber sagging; the fiber sags due to gravity toward the bottom piston, and a symmetric pattern is not to be expected from an effect with clear directionality. As mentioned before, the relative amount of β-iPP becomes negligible at the center of the fiber. Due to the relatively large spot size of the X-ray beam, it cannot be determined whether in the theoretical mid-point of the fiber, β-phase is present or that the measured value is simply a convolution of a larger exposed area.

Deduced from the residual orientation measured by SAXS, it could be hypothesized that chain alignment increases from the center to the tip of the fiber; a high molecular orientation can give rise to the formation of α-row nuclei, and since aligned α-row nuclei give rise to the formation of β-nuclei, the relative crystal phase content of β-iPP increases toward the tips as

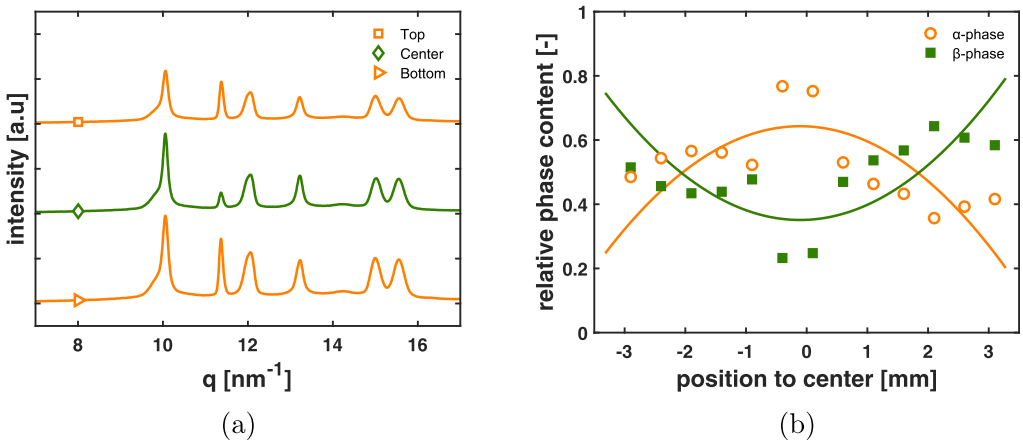

Figure 12. (a) Normalized WAXD integrated intensity patterns at three different positions of a one-dimensional scan in the z-direction. The top (1), center (2), and bottom (3) positions around the glass fiber in the neat iPP filament are located, and a measurement is taken after the complete crystallization of the filament. The samples are elongated to a true strain of 3 at a strain rate of 1 s^{-1} and a temperature of 133 °C. (b) Relative crystal phase content $\chi_{r,I}$ between α- and β-phase around the center of the fiber. Hereto, a one-dimensional scan is performed along the fiber center in the z-direction. The symbols present the measurements, and solid lines are visual guidelines.

https://doi.org/10.1021/acs.macromol.3c02632
Macromolecules 2024, 57, 2246−2259

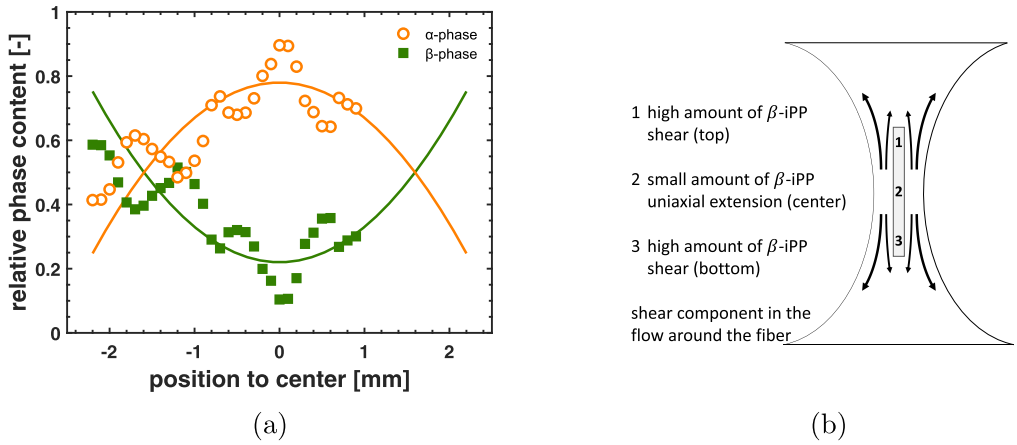

(a) (b)

Figure 13. (a) Relative crystal phase content $\chi_{r,i}$ between α- and β-iPP around the center of the fiber in a neat iPP filament. Hereto, a one-dimensional scan is performed along the filament center in the z-direction. The samples are elongated to a true strain of 3 at a strain rate of 1 s^{-1} and a temperature of 133 °C. The symbols present the measurements, and solid lines are visual guidelines. (b) Schematic representation of the flow field around such fiber, where the arrows represent the velocity gradient in the fluid due to the presence of the fiber. The numbers 1, 2, and 3 indicate the top, center, and bottom positions around the fiber, respectively.

well,[32] suggesting a transition from a transcrystalline to a columnar structure when going from the center to the tips of the fiber. The density of β-nuclei is increased from the center to the tips, and as the β-nuclei are more closely situated on the fiber interface, so are the β-phase crystals that grow from them. An increased restriction of growth to the lateral surface of the fiber is created due to the increasing packing density. The β−β impingement lines become closer positioned to one another, causing the amount of lamellar orientation to increase.

The hypothesis described above requires a closer look at the flow field around the fiber. In a filament without a fiber, an ideal uniaxial extension is found in the mid-filament point.[41] However, no distinctive orientation of the chains, neither during stretching nor in the crystallization afterward, is observed. Upon the introduction of a fiber, due to the symmetry of the flow (when gravity is neglected) in the mid-fiber position, the flow is still ideal uniaxial extension, as schematically represented in Figure 13b. On the other hand, at the fiber tips, the velocity gradient bifurcates. Part of the material flows outward to the free surface and part needs to move toward the central axis. Although the diameter of the fiber is small, recall 17 μm, this difference in velocity causes a velocity gradient which increases from the center to the tips of the fiber and creates additional shear components in the uniaxial elongation flow. It is believed that this shear is the responsible factor for the strong increase in β-phase at the interphase, which explains the increase in this phase content moving from the center toward the ends of the fiber.

To provide essential insight into the flow field, finite element method (FEM) modeling is performed and those results are able to explain the β-phase formation not only at the interphase but throughout almost the entire filament. On the lateral boundary of the fiber, two different cases are explored, namely, with a full slip and no-slip condition acting on the edge of the fiber. For both cases, the effect of gravity has been considered. The flow-orientation parameter is visualized as a function of time for these four different cases (with a slip or no-slip condition on the edges of the fiber and with and without gravity) in Figure 14. Here, the area around from the mid-filament to the tip of the fiber is presented, and the streamlines are colored by the value of the flow-orientation parameter. It should be recalled that a value of 1 implies pure uniaxial extension, whereas 0 determines a perfect shear flow and −1 a rigid body motion.[58]

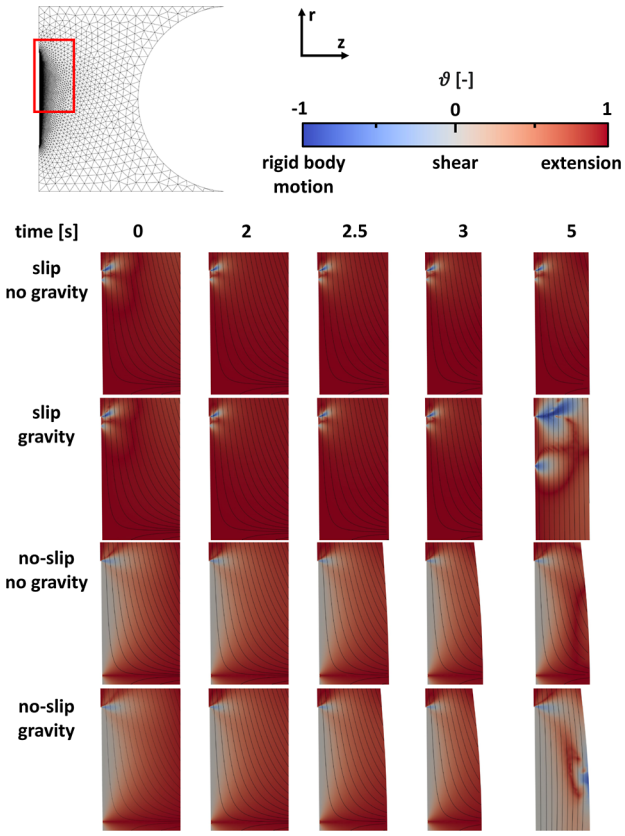

Figure 14. Zoom on the geometry of the simulations is presented for the cases with a slip or a no-slip condition on the interphase of the fiber, with and without taking gravity into account. The plots show the values of the flow-classification parameter ϑ over the geometry, and the streamlines are colored black. The filaments are stretched at a strain rate of 1 s^{-1} and a temperature of 133 °C to a true strain of 3. The geometries are shown at times of 0, 2, 2.5, 3, and 5 s.

For both conditions, gravity results in an asymmetric distribution of the flow type around the center after the flow is ceased, as can be seen at a time of 5 s (the flow time is 3 s).

https://doi.org/10.1021/acs.macromol.3c02632
Macromolecules 2024, 57, 2246−2259

This confirms the experimental observation where the fiber remains in the center during the flow and only shifts down afterward. In the simulations, immediately after the flow is stopped, the asymmetric distribution starts to develop; however, as relaxation is not taken into account by the fluid model used, a quantitative comparison to the experiments cannot be made.

Using a full slip boundary condition, the flow type is predominantly extension along the complete lateral surface of the fiber, similar to the simulation results without the fiber inclusion.[50,51] Only at the tip of the fiber a slight appearance of shear flow is present. The size of the shear area remains constant throughout the elongation of the filament. On the other hand, the no-slip condition gives rise to a substantial amount of shear. In the center, where the strain rate is controlled, an ideal uniaxial flow is located around the mid-fiber point. From the center to the tip of the fiber, the amount of shear increases. At the tip, a rapid transition appears from shear to rigid body motion, which passes on into an elongational flow moving toward the contact plates of the FiSER. Similar to the slip condition, the shear area remains constant during the elongation of the filament.

The flow around the fiber is evidently influenced by the no-slip condition, causing a velocity gradient in the radial direction that creates shear components in the flow, especially around the fiber/matrix interface. Combined with the experimental results presented here for uniaxial extension and the previously reported data on shear flow,[38] it can be confidently claimed that the essential element for the formation of β-phase polypropylene is a shear component in the flow. For an injection molding-grade iPP, a shear flow is more effective into crystallizing oriented structures as compared to a uniaxial elongation flow of similar strength. It should be noted that in practice, a perfect no-slip condition does not occur, and the actual situation is in-between a slip and no-slip case. The increased adhesion between fiber and matrix by the addition of matrix-compatibilized MAH-*g*-PP increases the interaction, but due to faster bulk crystallization kinetics, the formation of β-phase is hindered.

■ CONCLUSIONS

The morphology development around a single glass fiber in an iPP matrix upon uniaxial extension has been examined. In situ X-ray experiments during elongational flow have been conducted for the neat polymer matrix as well as samples containing a single glass fiber. The experiments show that for both the pure iPP and the MAH-*g*-PP-compatibilized iPP matrix, mainly α-phase crystals form, in contrary to earlier findings of structure development during shear flow. In addition, no significant chain alignment or formation of oriented structures could be observed for either of the before-mentioned materials. However, similar to shear flow, iPP with a MAH-*g*-PP compatibilizer has a higher nucleation density, earlier onset of crystallization, and faster overall kinetics.

Remarkably, the introduction of a single glass fiber results in a distinct development of β-phase throughout the entire filament in a neat iPP matrix. Following the reasoning that β-crystals will only nucleate on aligned α-phase, it can be concluded that the presence of the fiber thus led to an increase in the alignment of α-nuclei, which induces the formation of β-nuclei. From the midpoint to the ends of the fiber, a clear increase of β-phase content could be observed. Besides this increase in trigonal-phase content, the degree of lamellar orientation is increased as well; toward the fiber ends, the area density of β-nuclei has increased, and consequently, the β−β impingement occurs at a smaller distance from the fiber surface restricting the growth of each nucleus in the lateral direction, increasing the degree of orientation.

On the other hand, the addition of the single glass fiber to the MAH-*g*-PP-compatibilized iPP mainly prompts the growth of α-phase crystals. The adhesion modifier strongly accelerates the overall crystallization kinetics by increasing the nucleation density, therewith accelerating the space-filling. Hence, the formation of β-phase is suppressed as the available space already has been occupied by α-phase spherulites/super-structures.

Finite element simulations are performed to describe the flow field around a single fiber in a uniaxial elongational flow. Compared to the case where there is no inclusion, a substantial additional shear component is introduced, with a velocity gradient that increases from the center to the tip of the fiber, causing an increase in shear strength along the fiber surface. These shear components appear to dominate the flow both at the interphase as well as far away from the fiber surface and can explain the experimentally observed change in crystallizing polymorph and orientation. Apparently a shear component in the flow is essential for β-phase formation in iPP.

In an industrial application like tape extrusion, the macroscopic elongational flow is thus highly dominated by these local shear components. The perceived morphology, mechanically favored crystal phase, and crystallization kinetics may help to improve the performance of a final product. Generally, the developed morphology around a single glass fiber of an iPP matrix shows a transition from a transcrystalline structure in the center to a columnar structure at the tip of the fiber. The effects of improved fiber-matrix adhesion by the addition of the MAH-*g*-PP compatibilizer diminish the influence of shear flow around the fiber and hinder the formation of the mechanically preferred polymorph.

■ ASSOCIATED CONTENT

Supporting Information

The Supporting Information is available free of charge at https://pubs.acs.org/doi/10.1021/acs.macromol.3c02632.

Additional performed experiments (PDF)

■ AUTHOR INFORMATION

Corresponding Authors

Stan F. S. P. Looijmans − *Processing and Performance of Materials, Department of Mechanical Engineering, Eindhoven University of Technology, Eindhoven 5600 MB, The Netherlands; DPI, Eindhoven 5600 AX, The Netherlands;* orcid.org/0000-0002-4148-8351; Email: s.f.s.p.looijmans@tue.nl

Lambèrt C. A. van Breemen − *Processing and Performance of Materials, Department of Mechanical Engineering, Eindhoven University of Technology, Eindhoven 5600 MB, The Netherlands;* orcid.org/0000-0002-0610-1908; Email: l.c.a.v.breemen@tue.nl

Authors

Paul M. H. van Heugten − *Processing and Performance of Materials, Department of Mechanical Engineering, Eindhoven University of Technology, Eindhoven 5600 MB, The Netherlands;* orcid.org/0000-0002-6584-6440

https://doi.org/10.1021/acs.macromol.3c02632
Macromolecules 2024, 57, 2246−2259

Frank P. A. van Berlo − *Processing and Performance of Materials, Department of Mechanical Engineering, Eindhoven University of Technology, Eindhoven 5600 MB, The Netherlands*

Martin Rosenthal − *Department of Chemistry, KU Leuven, Leuven 3001, Belgium;* orcid.org/0000-0001-6014-6050

Patrick D. Anderson − *Processing and Performance of Materials, Department of Mechanical Engineering, Eindhoven University of Technology, Eindhoven 5600 MB, The Netherlands*

Complete contact information is available at: https://pubs.acs.org/10.1021/acs.macromol.3c02632

Notes

The authors declare no competing financial interest.

■ ACKNOWLEDGMENTS

This research forms part of the research program of DPI, Project #815 PROFIT. Combined SAXS/WAXD experiments were performed on beamline BM26 at the European Synchrotron Radiation Facility (ESRF), Grenoble, France. The authors are grateful to all DUBBLE staff for providing assistance in using beamline BM26. In addition, the authors thank Bjorn Tuerlings from PTG/e for his assistance with compounding the materials, dr.ir. Martien A. Hulsen (TU/e) for providing access to the toolkit for the Finite Element software TFEM, Lucien Cleven (TU/e) for the technical support, ir. Thijs R.N. Egelmeers (TU/e) for his assistance in making the CT-scan, and Hamid Ahmadi (TU/e) and prof.dr.ir. Ruth M. Cardinaels (TU/e and KU Leuven) for the assistance during the performed X-ray experiments.

■ REFERENCES

(1) Galli, P.; Danesi, S.; Simonazzi, T. Polypropylene based polymer blends: Fields of application and new trends. *Polym. Eng. Sci.* **1984**, *24*, 544−554.

(2) Tadmor, Z. Molecular orientation in injection molding. *J. Appl. Polym. Sci.* **1974**, *18*, 1753−1772.

(3) Münstedt, H. Extensional Rheology and Processing of Polymeric Materials. *Int. Polym. Process.* **2018**, *33*, 594−618.

(4) Morrison, F. A. *Understanding Rheology*; Oxford University Press: New York, 2001; pp 105−130.

(5) Goff, J.; Whelan, T. *The Dynisco Extrusion Processors Handbook*, 2nd ed.; De Laney, D., Ed.; Dynisco: New York, 2000; pp 1−36.

(6) Ramsteiner, F.; Theysohn, R. Tensile and impact strengths of unidirectional, short fibre-reinforced thermoplastics. *Composites* **1979**, *10*, 111−119.

(7) Várdai, R.; Lummerstorfer, T.; Pretschuh, C.; Jerabek, M.; Gahleitner, M.; Faludi, G.; Móczó, J.; Pukánszky, B. Comparative study of fiber reinforced PP composites: Effect of fiber type, coupling and failure mechanisms. *Compos. Appl. Sci. Manuf.* **2020**, *133*, 105895.

(8) Fu, S. Y.; Hu, X.; Yue, C. Y. Effects of fiber length and fiber orientation distributions on the tensile strength of short-fiber-reinforced polymers. *J. Soc. Mater. Sci., Jpn.* **1999**, *48*, 74−83.

(9) Fu, S.-Y.; Lauke, B.; Mäder, E.; Yue, C.-Y.; Hu, X. Tensile properties of short-glass-fiber- and short-carbon-fiber-reinforced polypropylene composites. *Compos. Appl. Sci. Manuf.* **2000**, *31*, 1117−1125.

(10) Zhang, K.; Guo, Q.; Zhang, D.; Guo, J. Mechanical Properties and Morphology of Polypropylene/Polypropylene-g-Maleic Anhydride/Long Glass Fiber Composites. *J. Macromol. Sci., Part B* **2015**, *54*, 286−294.

(11) Fu, X.; He, B.; Chen, X. Effects of Compatibilizers on Mechanical Properties of Long Glass Fiber-Reinforced Polypropylene. *J. Reinf. Plast. Compos.* **2010**, *29*, 936−949.

(12) Tjong, S. C.; Xu, S.-A.; Li, R. K.-Y.; Mai, Y.-W. Mechanical behavior and fracture toughness evaluation of maleic anhydride compatibilized short glass fiber/SEBS/polypropylene hybrid composites. *Compos. Sci. Technol.* **2002**, *62*, 831−840.

(13) Roozemond, P. C.; van Drongelen, M.; Ma, Z.; Hulsen, M. A.; Peters, G. W. M. Modeling flow-induced crystallization in isotactic polypropylene at high shear rates. *J. Rheol.* **2015**, *59*, 613−642.

(14) Roozemond, P. C.; van Erp, T. B.; Peters, G. W. Flow-induced crystallization of isotactic polypropylene: Modeling formation of multiple crystal phases and morphologies. *Polymer* **2016**, *89*, 69−80.

(15) Felix, J. M.; Gatenholm, P. Effect of transcrystalline morphology on interfacial adhesion in cellulose/polypropylene composites. *J. Mater. Sci.* **1994**, *29*, 3043−3049.

(16) Maddah, H. A. Polypropylene as a Promising Plastic: A Review. *Am. J. Polym. Sci.* **2016**, *6*, 1−11.

(17) Folkes, M. J.; Hardwick, S. T. The mechanical properties of glass/polypropylene multilayer laminates. *J. Mater. Sci.* **1990**, *25*, 2598−2606.

(18) Thomason, J. The influence of fibre length and concentration on the properties of glass fibre reinforced polypropylene: 5. Injection moulded long and short fibre PP. *Compos. Appl. Sci. Manuf.* **2002**, *33*, 1641−1652.

(19) Watanabe, R.; Sugahara, A.; Hagihara, H.; Mizukado, J.; Shinzawa, H. Molecular-scale deformation of glass-fiber-reinforced polypropylene probed by rheo-optical Fourier transform infrared imaging combined with a two-trace two-dimensional correlation technique. *Polymer* **2022**, *241*, 124536.

(20) Gray, D. G. Transcrystallization of polypropylene at cellulose nanocrystal surfaces. *Cellulose* **2008**, *15*, 297−301.

(21) Koscher, E.; Fulchiron, R. Influence of shear on polypropylene crystallization: Morphology development and kinetics. *Polymer* **2002**, *43*, 6931−6942.

(22) Quan, H.; Li, Z. M.; Yang, M. B.; Huang, R. On transcrystallinity in semi-crystalline polymer composites. *Compos. Sci. Technol.* **2005**, *65*, 999−1021.

(23) Varga, J. β-Modification of isotactic polypropylene: preparation, structure, processing, properties, and application. *J. Macromol. Sci., Part B* **2002**, *41*, 1121−1171.

(24) Lotz, B.; Wittmann, J.; Lovinger, A. Structure and morphology of poly(propylenes): a molecular analysis. *Polymer* **1996**, *37*, 4979−4992.

(25) Brückner, S.; Meille, S. V.; Petraccone, V.; Pirozzi, B. Polymorphism in isotactic polypropylene. *Prog. Polym. Sci.* **1991**, *16*, 361−404.

(26) Jones, A. T.; Aizlewood, J. M.; Beckett, D. R. Crystalline forms of isotactic polypropylene. *Makromol. Chem.* **1964**, *75*, 134−158.

(27) Keith, H. D.; Padden, F. J.; Walter, N. M.; Wyckoff, H. W. Evidence for a Second Crystal Form of Polypropylene. *J. Appl. Phys.* **1959**, *30*, 1485−1488.

(28) Addink, E.; Beintema, J. Polymorphism of crystalline polypropylene. *Polymer* **1961**, *2*, 185−193.

(29) Portale, G.; Troisi, E. M.; Peters, G. W. M.; Bras, W. *Advances in Polymer Science*; Springer New York LLC, 2015; Vol. *277*, pp 127−165.

(30) van Erp, T. B.; Balzano, L.; Spoelstra, A. B.; Govaert, L. E.; Peters, G. W. Quantification of non-isothermal, multi-phase crystallization of isotactic polypropylene: The influence of shear and pressure. *Polymer* **2012**, *53*, 5896−5908.

(31) Grosso, G.; Troisi, E. M.; Jaensson, N. O.; Peters, G. W.; Anderson, P. D. Modelling flow induced crystallization of IPP: Multiple crystal phases and morphologies. *Polymer* **2019**, *182*, 121806.

(32) Varga, J.; Karger-Kocsis, J. Interfacial morphologies in carbon fibre-reinforced polypropylene microcomposites. *Polymer* **1995**, *36*, 4877−4881.

(33) Folkes, M. J.; Hardwick, S. T. Direct study of the structure and properties of transcrystalline layers. *J. Mater. Sci. Lett.* **1987**, *6*, 656−658.

(34) Varga, J.; Karger-Kocsis, J. Direct evidence of row-nucleated cylindritic crystallization in glass fiber-reinforced polypropylene composites. *Polym. Bull.* **1993**, *30*, 105−110.
(35) Varga, J. Supermolecular structure of isotactic polypropylene. *J. Mater. Sci.* **1992**, *27*, 2557−2579.
(36) Varga, J.; Karger-Kocsis, J. The occurrence of transcrystallization or row-nucleated cylindritic crystallization as a result of shearing in a glass-fiber-reinforced polypropylene. *Compos. Sci. Technol.* **1993**, *48*, 191−198.
(37) Wu, C. M.; Chen, M.; Karger-Kocsis, J. Micromorphologic feature of the crystallization of isotactic polypropylene after melt-shearing. *Polym. Bull.* **1998**, *41*, 493−499.
(38) Looijmans, S. F. S. P.; Cavallo, D.; Merino, D. H.; Martinez, J. C.; Anderson, P. D.; Breemen, L. C. A. v. Shear-Induced Structure Formation in MAH-g-PP Compatibilized Polypropylenes. *Macromolecules* **2023**, *56*, 5278−5289.
(39) Etcheverry, M.; Barbosa, S. E. Glass Fiber Reinforced Polypropylene Mechanical Properties Enhancement by Adhesion Improvement. *Materials* **2012**, *5*, 1084−1113.
(40) Thomason, J. Glass fibre sizing: A review. *Compos. Appl. Sci. Manuf.* **2019**, *127*, 105619.
(41) Pepe, J.; Cleven, L. C.; Suijkerbuijk, E. J.; Dekkers, E. C.; Hermida-Merino, D.; Cardinaels, R.; Peters, G. W.; Anderson, P. D. A filament stretching rheometer for in situ X-ray experiments: Combining rheology and crystalline morphology characterization. *Rev. Sci. Instrum.* **2020**, *91*, 073903.
(42) Román Marín, J. M.; Huusom, J. K.; Alvarez, N. J.; Huang, Q.; Rasmussen, H. K.; Bach, A.; Skov, A. L.; Hassager, O. A control scheme for filament stretching rheometers with application to polymer melts. *J. Non-Newtonian Fluid Mech.* **2013**, *194*, 14−22.
(43) Bras, W.; Dolbnya, I.; Detollenaere, D.; van Tol, R.; Malfois, M.; Greaves, G.; Ryan, A.; Heeley, E. Recent experiments on a small-angle/wide-angle X-ray scattering beam line at the ESRF. *J. Appl. Crystallogr.* **2003**, *36*, 791−794.
(44) Hammersley, A. P.; Svensson, S. O.; Hanfland, M.; Fitch, A. N.; Hausermann, D. Two-dimensional detector software: From real detector to idealised image or two-theta scan. *High Pres. Res.* **1996**, *14*, 235−248.
(45) Hammersley, A. P. *FIT2D: An Introduction and Overview*, 1997.
(46) Hammersley, A. P. *FIT2D V9.129 Reference Manual V3.1*, 1998.
(47) Stribeck, N. *X-Ray Scattering of Soft Matter*, 1st ed.; Springer Berlin Heidelberg, 2007; pp 73−94.
(48) Zhang, H.; Scholz, A. K.; De Crevoisier, J.; Vion-Loisel, F.; Besnard, G.; Hexemer, A.; Brown, H. R.; Kramer, E. J.; Creton, C. Nanocavitation in carbon black filled styrene-butadiene rubber under tension detected by real time small angle X-ray scattering. *Macromolecules* **2012**, *45*, 1529−1543.
(49) Caelers, H. J.; Troisi, E. M.; Govaert, L. E.; Peters, G. W. Deformation-induced phase transitions in iPP polymorphs. *Polymers* **2017**, *9*, 547−586.
(50) van Berlo, F. P. A.; Cardinaels, R.; Peters, G. W.; Anderson, P. D. A numerical study of extensional flow-induced crystallization in filament stretching rheometry. *Polym. Cryst.* **2021**, *4*, No. e10154.
(51) van Berlo, F. P.; Cardinaels, R.; Peters, G. W.; Anderson, P. D. Towards a universal shear correction factor in filament stretching rheometry. *Rheol. Acta* **2021**, *60*, 691−709.
(52) Liu, C. Y.; He, J.; Keunings, R.; Bailly, C. New linearized relation for the universal viscosity - Temperature behavior of polymer melts. *Macromolecules* **2006**, *39*, 8867−8869.
(53) Hirt, C.; Amsden, A.; Cook, J. An arbitrary Lagrangian-Eulerian computing method for all flow speeds. *J. Comput. Phys.* **1974**, *14*, 227−253.
(54) Geuzaine, C.; Remacle, J. Gmsh: A 3-D finite element mesh generator with built-in pre- and post-processing facilities. *Int. J. Numer. Methods Eng.* **2009**, *79*, 1309−1331.
(55) Jaensson, N.; Hulsen, M.; Anderson, P. Stokes−Cahn−Hilliard formulations and simulations of two-phase flows with suspended rigid particles. *Comput. Fluid* **2015**, *111*, 1−17.
(56) Park, J. M. Flow classification of radial and squeeze flows between parallel disks. *J. Non-Newtonian Fluid Mech.* **2020**, *286*, 104416.
(57) Thompson, R. L.; Souza Mendes, P. R. Persistence of straining and flow classification. *Int. J. Eng. Sci.* **2005**, *43*, 79−105.
(58) Comminal, R.; Spangenberg, J.; Hattel, J. H. Robust simulations of viscoelastic flows at high Weissenberg numbers with the streamfunction/log-conformation formulation. *J. Non-Newtonian Fluid Mech.* **2015**, *223*, 37−61.
(59) Looijmans, S. F. S. P.; Spanjaards, M. M. A.; Puskar, L.; Cavallo, D.; Anderson, P. D.; van Breemen, L. C. A. Synergy of Fiber Surface Chemistry and Flow: Multi-Phase Transcrystallization in Fiber-Reinforced Thermoplastics. *Polymers* **2022**, *14*, 4850.
(60) Avrami, M. Kinetics of phase change. I: General theory. *J. Chem. Phys.* **1939**, *7*, 1103−1112.
(61) Avrami, M. Kinetics of Phase Change. II Transformation-Time Relations for Random Distribution of Nuclei. *J. Chem. Phys.* **1940**, *8*, 212−224.
(62) Avrami, M. Granulation, Phase Change, and Microstructure Kinetics of Phase Change. III. *J. Chem. Phys.* **1941**, *9*, 177−184.
(63) Supaphol, P.; Dangseeyun, N.; Srimoaon, P.; Nithitanakul, M. Nonisothermal melt-crystallization kinetics for three linear aromatic polyesters. *Thermochim. Acta* **2003**, *406*, 207−220.
(64) Vasile, C. *Handbook of Polyolefins*, 2nd ed.; Taylor & Francis, 2000; p 238.
(65) McKinley, G. H.; Sridhar, T. Filament-stretching rheometry of complex fluids. *Annu. Rev. Fluid. Mech.* **2002**, *34*, 375−415.
(66) Yao, M.; McKinley, G. H. Numerical simulation of extensional deformations of viscoelastic liquid bridges in filament stretching devices. *J. Non-Newtonian Fluid Mech.* **1998**, *74*, 47−88.

https://doi.org/10.1021/acs.macromol.3c02632
Macromolecules 2024, 57, 2246−2259